Optimization of a customized Simultaneous Algebraic Reconstruction Technique algorithm for phase-contrast breast computed tomography

S Donato[1,2], L Brombal[3,*], L M Arana Peña [3,4,5], F Arfelli[3,4], A Contillo[5], P Delogu[6,7], F Di Lillo[5], V Di Trapani[4], V Fanti[8,9], R Longo[3,4], P Oliva[9,10], L Rigon[3,4], L Stori[8], G Tromba[5] and B Golosio[8,9]

[1] Department of Physics, University of Calabria, 87036 Arcavacata di Rende (CS), Italy
[2] INFN Division of Frascati, Italy
[3] INFN Division of Trieste, 34127 Trieste, Italy
[4] Department of Physics, University of Trieste, 34127 Trieste, Italy
[5] Elettra-Sincrotrone Trieste S.C.p.A., 34149 Trieste, Italy
[6] Department of Physical Sciences, Earth and Environment, University of Siena, 53100 Siena (SI), Italy
[7] INFN Division of Pisa, 56127 Pisa, Italy
[8] Department of Physics, University of Cagliari, 09042 Monserrato (CA), Italy
[9] INFN Division of Cagliari, 09042 Monserrato (CA), Italy
[10] Department of Chemistry and Pharmacy, University of Sassari, 07100 Sassari, Italy

E-mail: * luca.brombal@ts.infn.it

July 2021

Abstract.
Objective: To introduce the optimization of a customized GPU-based simultaneous algebraic reconstruction technique (cSART) in the field of phase-contrast breast computed tomography (bCT). The presented algorithm features a 3D bilateral regularization filter that can be tuned to yield optimal performance for clinical image visualization and tissues segmentation.
Approach: Acquisitions of a dedicated test object and a breast specimen were performed at Elettra, the Italian synchrotron radiation (SR) facility (Trieste, Italy) using a large area CdTe single-photon counting detector. Tomographic images where obtained at 5 mGy of mean glandular dose, with a 32 keV monochromatic X-ray beam in the free-space propagation mode. Three independent algorithm's parameters were optimized by using contrast-to-noise ratio (CNR), spatial resolution, and noise texture metrics. The results obtained with the cSART algorithm were compared with conventional SART and filtered back projection (FBP) reconstructions.
Main results: Compared to conventional FBP reconstructions, results indicate that the proposed algorithm can yield images with a higher CNR (by 35% or more), retaining a high spatial resolution while preserving their textural properties. Alternatively, at the cost of an increased image "patchiness", the cSART can be tuned to achieve a high-quality tissue segmentation, suggesting the possibility of performing an accurate

glandularity estimation potentially of use in the realization of realistic 3D breast models starting from low radiation dose images.

Significance: The study indicates that dedicated iterative reconstruction techniques could provide significant advantages in phase-contrast bCT imaging. The proposed algorithm offers great flexibility in terms of image reconstruction optimization, either towards diagnostic evaluation or towards image segmentation.

Keywords: Breast CT, Propagation-based Phase-Contrast imaging, Iterative reconstruction algorithm, synchrotron radiation

Submitted to: *Phys. Med. Biol.*

1. Introduction

X-ray breast computed tomography (bCT) is a fully 3D mammographic technique in which multiple low-dose projections are acquired over an angle of 180 degrees or more and then reconstructed through suitable algorithms (Chen & Ning 2002, Sarno et al. 2015, O'Connell et al. 2018). Even though the first clinical studies in bCT were published more than ten years ago (Lindfors et al. 2008), the integration of this technique into clinical practice has only recently started (Wienbeck et al. 2017). Preliminary clinical studies have suggested that bCT can provide a good visualization of both masses and microcalcifications with a radiation dose comparable to, or slightly higher than, conventional mammographic exams (Shim et al. 2020). Following the first generation of bCT scanners, which was based on cone beam geometry and flat panel detectors (Lindfors et al. 2010, O'Connell et al. 2010), a new generation of bCT systems based on fan beams and photon-counting detectors has been recently developed (Kalender et al. 2017), reducing the negative impact of scattered radiation in the final image and improving the system's dose efficiency.

In addition to conventional x-ray imaging that relies uniquely on the absorption properties of the sample, phase-contrast (PhC) imaging techniques have demonstrated improved visibility of low-contrast features in soft tissues (Wilkins et al. 1996, Mittone et al. 2018, Brombal 2020b). In this context, programs of phase-contrast bCT (PhC bCT) are under development at Elettra, the Italian synchrotron radiation (SR) facility (Trieste, Italy) (Longo et al. 2019) and at the Australian Synchrotron in Melbourne (Gureyev et al. 2019). The setup at Elettra includes a high-resolution CdTe photon-counting detector (Bellazzini et al. 2013) and it is based on the free-space propagation modality which is arguably the simplest phase-sensitive technique to implement, only requiring to increase the sample-to-detector distance to detect phase effects. Owing to the high coherence provided by a synchrotron source, this arrangement results in images with an enhanced contrast across interfaces (edge-enhancement) (Wilkins et al. 1996). The "edge-enhanced" images, or projections, are further processed via a phase-retrieval algorithm (Paganin et al. 2002). The combined effect of free-space propagation and phase retrieval results in a major decrease in image noise at similar contrast and spatial resolution levels that would be observed in a conventional x-ray attenuation-based tomography (Gureyev et al. 2017, Brombal et al. 2018a, Baran et al. 2017). As recently demonstrated, the image quality of PhC bCT outperforms clinical bCT systems, providing a higher spatial resolution, signal-to-noise ratio and a finer granularity (Brombal et al. 2019, Pacilè et al. 2019). With the goal of setting up a clinical study, the SYRMA-3D collaboration has ~~worked~~ been working in the last years to evaluate, quantify and optimize the main parameters of the PhC bCT imaging technique in terms of x-ray energy (Delogu et al. 2019, Oliva et al. 2020), sample-to-detector distance (Brombal et al. 2018b, Brombal 2020a), detector's operating mode, strategies for CT scans and reconstruction workflow (Longo et al. 2019, Brombal et al. 2021).

Breast compute tomography must provide high spatial and contrast resolution with a radiation dose level comparable to a standard 2-view mammography. Low radiation dose can be achieved either by reducing the x-ray fluence per tomographic projection (Greffier et al. 2015, Solomon et al. 2017) or by decreasing the number of projections (Sidky et al. 2014). The first approach, while preserving a good angular sampling, results in an increased noise in the projection images leading to a noisier CT image. Conversely, when the number of projections falls significantly below the Nyquist angular sampling criterion, analytical reconstruction algorithms introduce significant image artefacts and, again, increased noise. Several approaches have been proposed to improve the global image quality in low dose CT scans and some of them have been applied to bCT data (Zhao et al. 2012), including iterative reconstruction (IR) algorithms (Sidky & Pan 2008, Makeev & Glick 2013, Bian et al. 2014, Pacilè et al. 2015, Delogu et al. 2017a).

IR techniques usually search for a smooth/regular solution compatible with the measured projection data and, for some algorithms, that satisfies other additional constraints (e.g., non-negativity). Thanks to the advancements in terms of computational power, IRs are attracting a growing interest in many applications of biomedical x-ray imaging (Löve et al. 2013, Nishiyama et al. 2016). Multiple clinical studies have shown their potential in terms of image quality improvement and/or radiation dose reduction when compared against the standard filtered back projection (FBP) or Feldkamp-Davis-Kress reconstructions (Gervaise et al. 2012, Willemink et al. 2013, Löve et al. 2013, Chen et al. 2014a, Mirone et al. 2014, Greffier et al. 2015, Nishiyama et al. 2016). Additionally, the integration of regularization filters within IR techniques enables both a noise reduction in homogeneous regions of the image (low spatial frequency component) and the preservation of details across interfaces (high spatial frequency component). On the other hand, IRs are generally associated with an undesired change in the image texture, described by radiologists as "patchy" (Chen et al. 2014b, Schulz et al. 2013), in some cases leading to a negative impact on their clinical implementation (Miéville et al. 2013). The image "patchiness" can be understood quantitatively as an increment of noise spatial correlation, described by a shift towards the lower spatial frequencies of the noise power spectrum (NPS) peak when compared to the FBP case.

In this framework, the reconstruction algorithm optimization represents one of the last steps of the SYRMA-3D project towards the clinical implementation of PhC bCT aiming to improve the global image quality for clinical compatible low dose CT scans, i.e. below 5 mGy of total mean glandular dose (MGD) (Fedon et al. 2015, Mettivier et al. 2015). In this study we describe and use a custom-made GPU-based simultaneous algebraic reconstruction technique (cSART) in combination with a 3D bilateral regularization filter. Compared to other iterative algorithms, SART generally ensures a fast convergence and flexibility allowing the implementation of custom modifications ~~. Moreover, SART~~ , it is easily parallelizable on GPU and it is usually associated with noise reduction while preserving the sharpness of edges and interfaces. It should also be remarked that, despite this study being focused on SART due to its straightforward implementation, the bilateral filter can be in principle integrated within any iterative reconstruction algorithm. To date only few specific studies on IRs dedicated to bCT have been published (Oliva et al. 2017, Tseng et al. 2020) and most of clinical applications reported in the literature rely on analytical reconstructions. The proposed cSART algorithm requires the tuning of 3 independent parameters, providing a higher flexibility with respect to the standard SART (Gordon et al. 1970, Kak et al. 2002). Specifically, following the preliminary results published in (Donato et al. 2019a), the effect of these parameters on noise power spectrum (NPS), spatial resolution and contrast-to-noise ratio (CNR) are herein discussed and, by analyzing the peak frequency of the NPS curve, optimal combinations of parameters preserving the image texture are identified for the PhC bCT system at hand. Moreover, the possibility of obtaining suitable images for tissue segmentation is investigated. This task can be of great interest for the glandularity assessment and for the realization of realistic virtual (Caballo et al. 2018) or 3D printed (Germann et al. 2020) breast phantoms. The imaging results obtained with the cSART algorithm are ~~also~~ compared with conventional SART and FBP reconstructions.

2. Materials and methods

2.1. Samples description

The presented study is based on images of two samples: i) a breast mastectomy with a maximum diameter of 9 cm and a vastly differentiated infiltrating ductal carcinoma (already described in (Piai et al. 2019)); ii) a bCT dedicated test object (Contillo et al. 2018, Piai et al. 2019) composed by a polymethyl methacrylate (PMMA) cylindrical container (diameter 12 cm, height 10 cm) filled with demineralized water and a set of five plastic rods (diameter 1.2 cm) made of polyethylene (PE), nylon, polyoxymethylene (POM), polytetrafluoroethylene (PTFE) and BR12 breast-tissue equivalent material, respectively. These materials were chosen to mimic the attenuation and contrast of breast tissues. The test object's design allows to image the plastic rods, for CNR and spatial resolution measurements, and the uniform water background, located at a different vertical position, for NPS evaluation. Prior to the CT scan, the mastectomy sample was fixed in formalin and sealed in a vacuum bag. The handling of the specimen followed the Directive 2004/23/EC of the European Parliament and of the Council of 31 March 2004 on setting standards of quality and safety for the donation, procurement, testing, processing, preservation, storage, and distribution of human tissues. The images were acquired in the framework of the operative protocol of the Breast Unit of the Trieste University Hospital ("PDTA Neoplasia mammaria", approved on 11 December 2019 by ASUGI—Azienda Sanitaria Universitaria Giuliano Isontina, Italy). A written informed consent was obtained from the patient prior to her inclusion into the study. The specialized breast center of ASUGI is in compliance with the standard of EUSOMA guidelines (certificate No. 1027/01).

2.2. Beamline description and experimental setup

Images were collected at the SYRMEP beamline (Tromba et al. 2010) of the Elettra synchrotron facility, with the storage ring operating at 2.4 GeV. X-rays are produced by a bending magnet and they can be monochromatized in the range 8.5-40 keV by means of a Si(111) double-crystal monochromator, providing an energy resolution of approximatevely 0.1%. Samples were positioned in a pendant geometry hanging from the patient support, a rotating table with an ergonomically designed aperture at the rotation center, 30 m away from the source. At sample position the x-ray beam had a laminar shape with a cross section of 220 mm (horizontal) $\times$ 3.5 mm (vertical, Gaussian shape, full width half maximum), while the object-to-detector distance was set to 1.6 m. Images were collected with a CdTe photon-counting detector (Pixirad-8) (Bellazzini et al. 2013, Delogu et al. 2017b) featuring a 60 μm pixel pitch and a global active area of 246 mm $\times$ 24.8 mm, leading to a matrix of 4096 $\times$ 476 pixels. Samples were scanned in continuous rotation by acquiring 1200 evenly spaced projections over 180° at a rate of 30 Hz. The beam energy was set to 32 keV while the beam intensity was adjusted by means of aluminium filters to deliver 5 mGy of total MGD.

2.3. Image Reconstruction

Projection images were pre-processed through a detector-specific procedure (Brombal et al. 2018c) and phase-retrieved prior to tomographic reconstruction (Brombal et al. 2018b, Donato et al. 2019b). The well-known phase-retrieval algorithm based on the homogeneous transport of intensity equation (TIE-Hom) (Paganin et al. 2002) was used, selecting a δ/β value of 2308, which corresponds to (ICRU-44) breast tissue (White et al. 1989), as reported in a publicly available database (Taylor 2018). Phase-retrieved projections were reconstructed with a GPU-based FBP and Shepp-Logan filtering, a standard SART with 5 iterations (both part of the Astra toolbox for tomography (Van Aarle et al. 2016)) and the cSART algorithm introduced in the next section. In addition to the Shepp-Logan filtering, that is standard in many bCT applications (Shim et al. 2020, Brombal et al. 2019), reconstructions with different common FBP filters were performed. Namely, from the sharpest to the smoothest, Ram-Lak, Cosine and Hamming and Hann, filters were used while the respective results reported in the supplementary material. Reconstructions were performed on a system equipped with a GPU NVIDIA® GeForce RTX 2080 Ti card with 11 GB of GDDR6 VRAM, 4352 CUDA cores, and a boost clock of 1.635 MHz. The reconstruction time for each slice was: 25 s for the cSART, 21 s for the standard SART and less than 1 s for FBP.

2.4. The custom SART algorithm

The customized version of the SART algorithm has been implemented to exploit parallel GPU computation performances by using the C++/CUDA programming language. In the standard SART algorithm iterative corrections are computed at each angular step (angle-by-angle) and they are evaluated and applied simultaneously to all the rays of the projection. One iteration is considered to be complete when all the projections have been used. As described in the following, the cSART implementation entails several improvements over the standard SART algorithm, ensuring higher flexibility to optimize the image quality (a detailed description of the algorithm can be found in Section S1 of the supplementary materials).

(i) The iterative corrections are weighed with a relaxation factor (Golosio et al. 2004), so that the update formula for the $(k+1)$-th iteration reads:

$$F^{(k+1)}(i_x, i_y) = F^{(k)}(i_x, i_y) + \eta^{(k)} C^{(k)}(i_x, i_y) \tag{1}$$

where $F^{(k)}$ is the image estimated at the k-th iteration and $C^{(k)}$ is the respective normalized image correction in the reconstruction plane (i_x, i_y). The relaxation factor η is applied to the corrections to reduce image noise in the reconstruction. In our implementation, η grows linearly from zero to a maximum η_{max} in the first few angular steps (in the current work this value was set to 10) then it decreases linearly with the number of iterations and angular steps down to zero for the last angular step of the last iteration. In this work we used $\eta_{max} = 0.5$.

(ii) Projections corresponding to different angles are used in random ordering scheme.

(iii) A bilateral 3D filter is applied periodically to the reconstructed image guess during the iterative process. In the filter, the content of each pixel is replaced with a weighted average accounting for both the (3D) Euclidean distance and the gray-level difference of neighbouring pixels. The used weighting kernels are Gaussian, so that the weight of the pixel identified with indices i'_x, i'_y, i'_z in filtering the pixel i_x,

i_y, i_z is:

$$K(i'_x, i'_y, i'_z; i_x, i_y, i_z) = \exp\Bigg[-\frac{(i'_x - i_x)^2 + (i'_y - i_y)^2}{2\sigma_{xy}^2} \dots \\ - \frac{(i'_z - i_z)^2}{2\sigma_z^2} - \frac{(F(i'_x, i'_y, i'_z) - F(i_x, i_y, i_z))^2}{2\sigma_v^2} \Bigg] \tag{2}$$

where σ_{xy}, σ_z and σ_v are parameters related to the spatial width of the filter in the horizontal plane, to the width in vertical direction, and to the width in content difference, respectively. $F(i'_x, i'_y, i'_z)$ and $F(i_x, i_y, i_z)$ are the contents of the pixels i'_x, i'_y, i'_z and i_x, i_y, i_z respectively, where x and y are the spatial coordinates in each projection image and z is the projection index. In this work σ_{xy} and σ_z are chosen to be equal and expressed in pixel size units, while σ_v is expressed in the same units as $F(i_x, i_y, i_z)$. By calling $\tilde{F}^{(k)}$ the image filtered with the kernel K, the reconstructed image is updated periodically during the iterative process as:

$$F^{(k)} \rightarrow (1 - w)F^{(k)} + w\tilde{F}^{(k)} \tag{3}$$

where w is a weighting factor comprised between 0 (no filtration) and 1 (full filtration).

To optimize the cSART parameters, images were reconstructed with different combinations of the algorithm's parameters, by varying $\sigma_{xy} = \sigma_z$ in the range [2 : 7] pixels with a step of 1 pixel, σ_v in the range [0.004 : 0.014] with step of 0.002 and ~~η_{max} (hereafter η)~~ w in the range [0.04 : 0.16] with step of 0.02, corresponding to a total of 252 reconstructions. Of note, we set $\sigma_{xy} = \sigma_z$, but in principle they can be different for a higher level of customization. The number of iterations was fixed to 5, consistently with the standard SART reconstructions, while the regularization filter was applied every 100 randomly ordered angular steps. Reconstructions were obtained with different numbers of iterations in the range [4 : 8]: in the main text only results corresponding to 5 iterations are shown, consistently with standard SART reconstructions, whereas results for different numbers of iterations are reported in the supplementary materials document. ~~Larger numbers of iterations were tested but generally they did not improve the reconstruction quality while increasing the processing time.~~

2.5. Quantitative assessment

The quantitative evaluation of cSART images was carried out in comparison with the FBP algorithm, assumed as reference, and with the standard SART algorithm. We firstly focused on the image texture by analysing the noise power spectrum. Then a quantitative evaluation was performed by using the contrast-to-noise ratio and spatial resolution metrics. Lastly, a further type of assessment involved the use of reconstructions for tissue segmentation. Images were analysed through dedicated MATLAB (The MathWorks, Inc., Natick, MA, United States) codes.

2.5.1. Noise Power Spectrum Image noise and texture were characterized by means of the noise power spectrum (NPS) (Verdun et al. 2015), which is the noise spectral decomposition in the Fourier space. For each reconstruction the 2D NPS map was measured from equally sized homogeneous ROIs according to the following definition:

$$NPS(f_x, f_y) = \frac{d_x d_y}{N_x N_y} \frac{1}{N_{ROI}} \sum_{i=1}^{N_{ROI}} \left| \mathcal{F}[I_i(x,y) - \overline{I}_i] \right|^2 \tag{4}$$

where f_x and f_y are the spatial frequencies, N_x and N_y are the ROI dimensions in number of pixels, d_x and d_y are the pixel dimensions in mm, N_{ROI} is the total number of selected ROIs, $\mathcal{F}$ denotes the 2D Fourier transform, $I_i(x,y)$ is the pixel value at position (x,y) of the $i-$th ROI, while $\overline{I}_i$ is the respective mean value. The corresponding image noise (σ) is obtained from the NPS as:

$$\sigma^2 = \int \int NPS(f_x, f_y) df_x df_y. \tag{5}$$

Given the radial symmetry of 2D NPS in CT reconstructions, 1D radially averaged NPS maps were also computed by using the identity $f_r^2 = f_x^2 + f_y^2$. Peak frequency (f_{peak}) of radial NPS curves were used for the determination of image texture, where a high peak frequency corresponds to a high granularity and a low peak frequency corresponds to a coarse noise, resulting in a patchy appearance. On the test object both 2D and 1D NPS distributions were evaluated by selecting in a homogeneous water region 25 non-overlapping circularly distributed square ROIs with an area of 0.72×0.72 mm^2, as shown in Fig. 1 (a). For the breast sample NPS measurements were performed over 10 homogeneous ROIs within the adipose tissue (black squares in Fig. 1 (c)) at nearly the same distance from the center of the specimen. Each ROI within the tissue have 64×64 pixels area (0.36×0.36 mm^2). To precisely determine their peak frequency, 1D NPS curves were oversampled by a factor of 4.

2.5.2. Contrast-to-noise ratio

The CNR was evaluated by using the following definition:

$$CNR = \frac{\overline{I_d} - \overline{I_b}}{\sqrt{(\sigma_d^2 + \sigma_b^2)/2}} \tag{6}$$

where $\overline{I_d}$ and $\overline{I_b}$ are the average pixel intensities of the detail d and the background b, while σ_d and σ_b are the respective standard deviations (i.e. noise). In the phantom the CNR of each plastic insert was measured with respect to the water background. A square ROI of 64×64 pixels was selected within each rod, while, for the background estimation, 10 evenly spaced ROIs were selected in the neighbouring region (see Fig. 1 (b)). The background's standard deviation was taken as the average of the background ROIs standard deviations. On the breast specimen CNR was measured as the average CNR value of three pairs of square ROIs selected within glandular (detail) and adipose (background) tissues, as shown by the green and red squares in Fig. 1 (c).

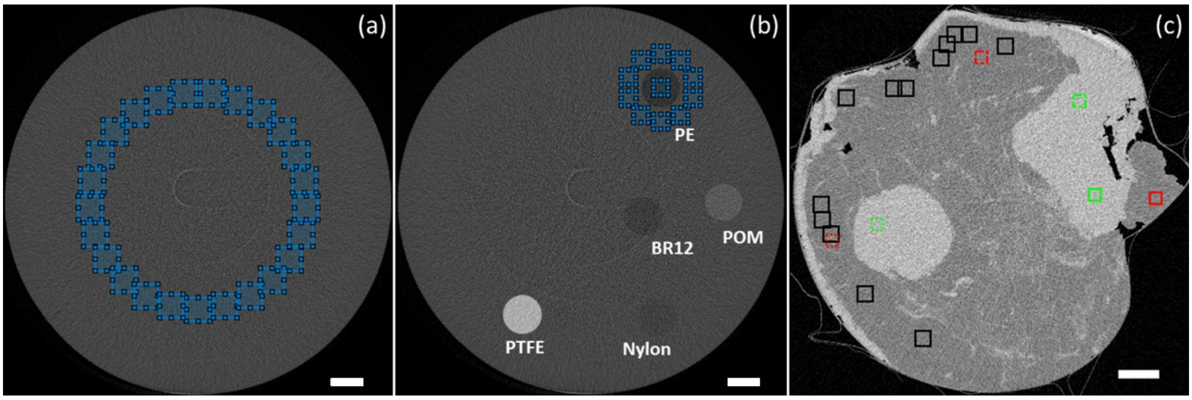

Figure 1. Homogeneous water-filled (a) and plastic details (b) regions of the test object. Blue squares represent the ROIs used to evaluate the NPS, in (a), and the CNR of the PE detail, in (b). Breast tissue reconstruction (c) where the ROIs for NPS (black squares), CNR (green squares for detail, red squares for background) are displayed. Scale bars correspond to 10 mm.

2.5.3. Spatial resolution In the test object the spatial resolution was characterized through the task transfer function (TTF), which is an object-dependent extension of the modulation transfer function (MTF) describing the spatial resolution for a specific object contrast and background noise (Li et al. 2014, Solomon et al. 2015). While MTF is usually measured on a single high-contrast detail, TTF is measured for various materials exhibiting different contrasts. TTF is useful in the characterization of non-linear/iterative algorithms where the spatial resolution is, in general, influenced by the image contrast level, meaning that different interfaces will show different levels of sharpness. It is worth noting that, when phase-retrieval filter is applied, this consideration applies also to FBP reconstructions and it will be discussed in more detail in subsection 3.1.2.

TTF was evaluated by using the circular edge method, which requires a polar coordinate transformation allowing to estimate the detail's edge-spread function from which TTF is derived (Richard et al. 2012, Chen et al. 2014b). TTF was measured on PE, Delrin and Teflon inserts whereas the contrast yielded by Nylon and BR12 inserts was insufficient for applying the circular edge method. Starting from the frequency corresponding to the 50% of the TTF curve ($f_{50\%}$), the spatial resolution was evaluated as the full width at half maximum (FWHM) of the corresponding point-spread function (PSF) (Bartels 2013):

$$FWHM(mm) = \frac{1}{2.26 \times f_{50\%}(lp/mm)} \tag{7}$$

where this equation holds in the Gaussian approximation for both TTF and PSF.

Due to the lack of sharp interfaces in the breast specimen the spatial resolution was estimated through an alternative procedure recently introduced by Mizutani *et al.* (Mizutani et al. 2016), which has already been applied to bCT images (Brombal et al. 2019). The main advantage of this approach, based on Fourier spectrum's fitting (Saiga et al. 2018), is that it allows to estimate the overall spatial resolution in terms of FWHM directly from general sample images, thus not requiring dedicated test objects. On the other hand, the model underlying this method contains the assumption of a Gaussian system's PSF, which is not rigorously true for many modern CT systems, is not material specific. In this context, Mizutani's method can be regarded as an approximate but easy way to assess spatial resolution from general samples images that is particularly useful for comparison studies. To cross-check the spatial resolution results, this technique is also applied to the test object images.

2.5.4. Segmentation and image comparison The last type of quantitative assessment in this study involved the tissue segmentation and the comparison against a high dose (50 mGy) ground-truth FBP reconstruction. Considering the breast tissue composition, a simple segmentation approach consists in using two thresholds, one for the separation of the background (air) and the other for the separation of glandular from adipose tissues. For the ground-truth image, which presents a low level of noise, the gray-level distributions of the tissue's components are well separated, so the segmentation thresholds were set at the local minima between each distributions pair. On the other hand, the gray-level distributions of adipose and glandular tissues in the low dose images present, in general, superposition, therefore requiring for a threshold optimization. The gray-level distributions of both ground-truth and low dose images are reported in Fig. S1 of the supplementary material.

The figure of merit chosen for the evaluation of segmentation quality and for the optimization of reconstruction parameters and segmentation thresholds was the macro-F1 score (Opitz & Burst 2019). This score is often used in multi-class classification problems (Wu & Zhou 2017, Lipton et al. 2014) and it is based on the image confusion matrix. In particular, let m_{ij} be the element i, j of the confusion matrix, where the second index j represents the ground-truth, while the first index i represents the output of the classification. In our application, m_{ij} is the number of pixels that belong to the class j in the segmented high-dose image and to the class i in the segmented low-dose image. Let P_i, R_i and $F1_i$ denote the precision, recall and F1 score for the class i:

$$P_i = \frac{m_{ii}}{\sum_j m_{ij}}; \quad R_i = \frac{m_{ii}}{\sum_j m_{ji}}; \quad F1_i = \frac{2P_iR_i}{P_i + R_i}. \tag{8}$$

The macro-F1 is computed as the arithmetic mean of the F1 scores of all the classes:

$$F1 = \frac{1}{n}\sum_i F1_i \tag{9}$$

where n is the number of classes. Given its definition, the values of F1 range from 0 to 1, with 1 indicating a segmentation identical to the ground truth. The optimal cSART reconstruction in terms of segmentation will be the one which maximizes F1 with respect to all the four free parameters, namely $\sigma_{xy,z}$, σ_v, η and the threshold th between glandular and adipose components. In this analysis the range of cSART reconstruction parameters has been further expanded by varying σ_{xy} and σ_z in the range [2 : 10] pixels with a step of 1 pixel, σ_v in the range ~~[0.004 : 0.020]~~ [0.004 : 0.030] with step of 0.002 and $\cancel{\eta}$ w in the range [0.04 : 0.20] with step of 0.02.

3. Results and discussion

3.1. Test Object

3.1.1. Noise power spectrum As stated in the introduction, the shift toward low frequencies of the NPS peak is followed by a change in the image texture demonstrated by Fig. 2. Panels (a)-(d) show homogeneous water ROIs reconstructed with FBP, cSART (with $\sigma_{xy,z} = 2$, $\sigma_v = 0.004$ and $\cancel{\eta}$ $w = 0.04$), cSART (with $\sigma_{xy,z} = 6$, $\sigma_v = 0.014$ and $\cancel{\eta}$ $w = 0.06$) and standard SART, respectively. Their respective 2D NPS plots are reported in color logarithmic scale in panels (e)-(h). The 2D NPS plots of FBP and cSART show a clear circular symmetry, while in the SART case a slightly higher noise contribution is observed along the Cartesian directions. From 2D NPS plots the average radial profiles are computed as shown in panel (i), resulting in peak frequencies of 0.89 mm^{-1}, 0.89 mm^{-1}, 0.44 mm^{-1} and 0.44 mm^{-1}, respectively. In terms of texture, it is clear that the cSART with low parameters values allows to produce images which are very similar to the reference FBP case, whereas larger values, as well as the use of standard SART, introduce more correlation resulting in a coarser noise. On the other hand, the cSART algorithm allows a reduction (by a factor larger than 2 with the largest parameters values) in the noise magnitude if compared with the FBP. Conversely, the standard SART yields a higher noise than FBP. Considering that in SART reconstructions the noise magnitude decreases for smaller iteration numbers, additional reconstructions have been performed with a decreasing number of iterations (from 5 to 1) but little differences (below 10%) in noise magnitude were found.

Focusing on the optimization of cSART parameters, panel (a) of Fig. 3 shows the radial NPS behaviour going from the smallest (noisiest image) to the largest (smoothest image) cSART parameter combination in comparison with the FBP case. Results considering reconstruction performed with FBP filters other than Shepp-Logan are reported in Fig. S2 (a) of the supplementary material. The double-arrow line indicates that the NPS peak frequency moves toward lower values as the image noise decreases. This behavior is further supported by the scatter plot in panel (b) where it is shown that the NPS peak frequency is strongly correlated with (as a first approximation linearly dependent to) the image noise magnitude. Moreover, having the possibility to finely modify the NPS peak frequency by tuning the cSART parameters, it is useful to define a threshold criterion to distinguish parameters preserving a noise texture similar to the FBP case from parameter sets yielding a coarse/patchy image appearance. Consequently, in panel (b) a threshold criterion has been introduced identifying images whose NPS peaks differ less than 15% from the FBP case (orange points). Despite

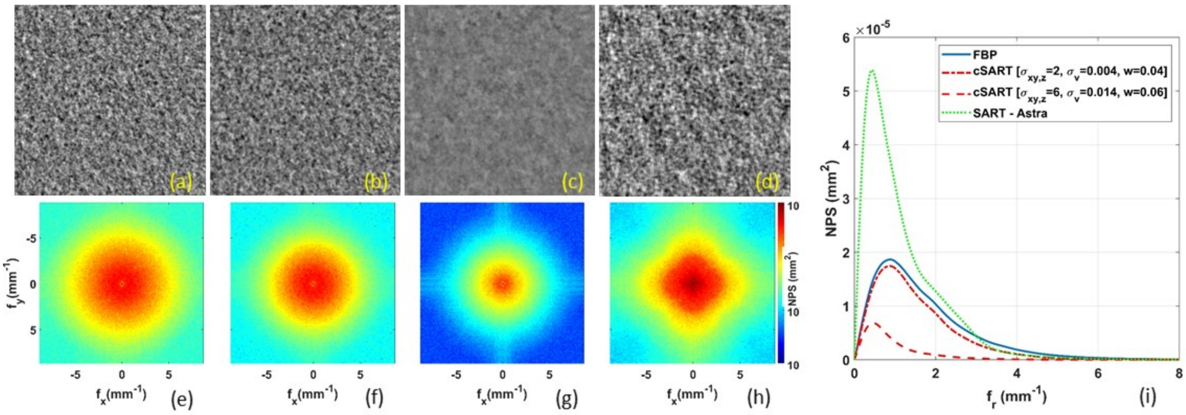

Figure 2. Homogeneous 256×256 pixel water ROIs obtained with FBP (a), cSART ($\sigma_{xy,z} = 2$, $\sigma_v = 0.004$, $\cancel{\eta}\ w = 0.04$) (b), cSART ($\sigma_{xy,z} = 6$, $\sigma_v = 0.014$, $\cancel{\eta}\ w = 0.06$) (c) and standard SART algorithm (d). In (e)-(h) the respective 2D NSP are reported in logarithmic color scale. In (i) the radial average NPS profiles for FBP (solid blue line), cSART (red dash/dash dotted lines) and standard SART (green dashed line).

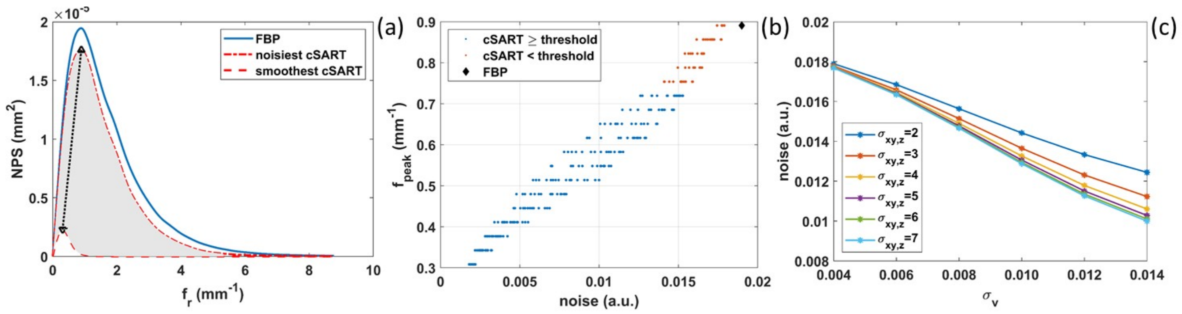

Figure 3. In (a) radial NPS curves measured from FBP (blue solid line), from cSART with the smallest parameter combination (red dot dashed line) and from cSART with the largest parameter combination (red dashed line). The gray shaded area represents the range of NPS curves obtained with intermediate cSART parameters. In (b) a scatter plot of the NPS frequency peaks as a function of the measured image noise: orange and blue points refer to reconstruction within and out of the NPS peak threshold criterion, respectively. The FBP result (black diamond) is reported for comparison, while standard SART (not shown) has frequency peak at 0.41 mm^{-1}. In (c) the image noise is plotted against the bilateral filter parameter σ_v, for different values of $\sigma_{xy,z}$ (different line colors) and at a fixed relaxation factor $\cancel{\eta}\ w = 0.04$.

being an arbitrary value and related to our imaging system, which can be in principle subject to dedicated optimization, this threshold is useful as a first line discrimination to rule out parameters yielding a too aggressive image filtration. Panel (c) shows the dependence of image noise versus the bilateral filter width σ_v for different values of $\sigma_{xy,z}$ at a fixed relaxation factor $\eta = 0.04$. From the figure it is clear that larger filter parameters monotonically bring to a lower image noise. The same consideration holds for increasing relaxation factor values. For this reason, each triplet of the cSART

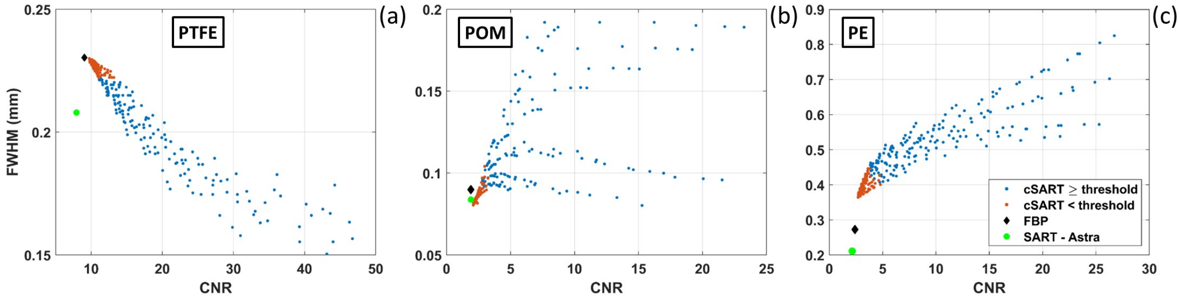

Figure 4. Scatter plots of the measured FWHM against the CNR across PTFE (a), POM (b) and PE (c) interfaces. Orange and blue points indicate cSART reconstructions within and out from the NPS peak threshold condition, respectively. Results of FBP (black diamond) and SART (green circle) are also reported.

parameters identifies the image filtration 'strength', where the increase of each single parameter brings to a lower noise magnitude and a lower NPS peak frequency. A similar behaviour has been discussed for other iterative filters used in clinical practice by a number of recent publications (Ghetti et al. 2013, Solomon et al. 2015, Euler et al. 2018).

3.1.2. Contrast-to-noise ratio and spatial resolution The scatter plots in Fig. 4 show the spatial resolution, measured with the circular edge technique, as a function of the CNR corresponding to the PTFE (a), POM (b) and PE (c) details, respectively, for the images reconstructed with cSART (dots), FBP (diamond marker) and SART (circular marker). Results for the different FBP filters are reported in Fig. S2 (b) of the supplementary material The results show that the use of cSART algorithm can yield a significant increase in CNR which, considering only the points within the threshold condition, is as high as 45%, 70% and 100% for PTFE, POM and PE details, respectively. In terms of spatial resolution, the cSART yields comparable or better results with respect to the FBP for the PTFE (a) and POM (b) details, while the resolution is degraded at the PE (c) interface by a 30% or more. Considering the trends of the cSART data for the different materials, it is interesting to observe that higher CNR values are associated with better spatial resolutions at PTFE interface (a) and with a generally worse resolutions at POM (b) and PE (c) interfaces. These different trends further justify the use of the TTF approach, as the results of the custom iterative reconstruction algorithm exhibit a material-specific behaviour. On the same topic, it should be noted that the FWHM broadly varies as a function of the interface also for FBP reconstructions, going from 0.09 mm for POM to 0.27 mm for PE. This effect, which should not be present in conventional attenuation-based CT, is due to the application of the phase-retrieval filter that is common to all the reconstructed images. In fact, the δ/β parameter of the phase-retrieval filter is material/interface specific. Since the scanned object is heterogeneous, the chosen δ/β cannot be optimal for all the interfaces

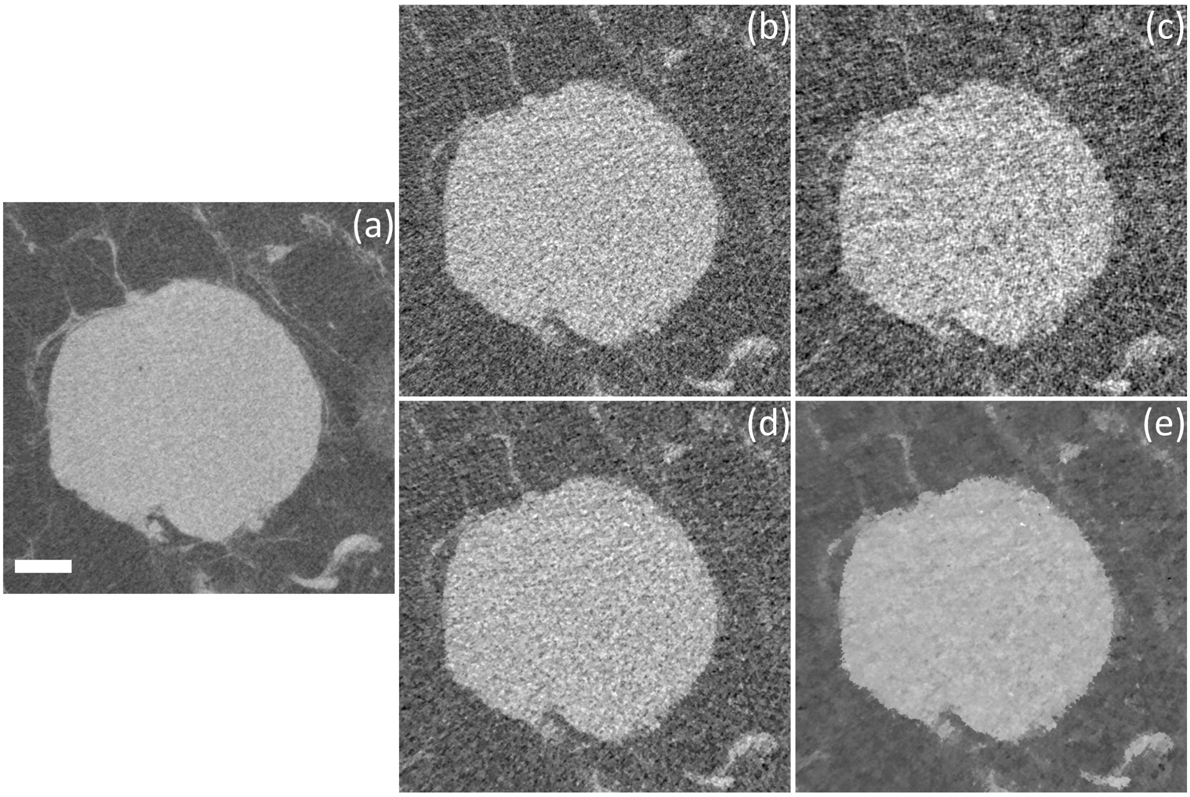

Figure 5. Breast sample detail depicting a tumor mass (light gray) in an adipose background (dark gray), acquired at 50 mGy MGD (a) and 5 mGy MGD (b)-(e). Reconstructions are performed with FBP in (a) and (b), standard SART in (c), cSART within the threshold condition in (d) and cSART out from the threshold condition in (e). Scalebar corresponds to 5 mm.

within the sample, resulting in an excessive blurring at the interfaces where δ/β is overestimated, and an enhanced sharpness due to uncompensated phase-contrast fringes at interfaces where δ/β is underestimated (Thompson et al. 2019). In our work, we set $\delta/\beta = 2308$, which corresponds to the breast tissue/air interface at 32 keV. On the other hand, the nominal δ/β values for the phantom inserts' interfaces with water are of 1448 for PTFE, 41765 for POM and 427 for PE, respectively. Considering that, from a signal processing perspective higher δ/β values correspond to higher smoothing due to the phase retrieval (Beltran et al. 2010, Brombal et al. 2018b, Donato et al. 2019b), it is clear that the POM interface is under-smoothed, yielding the best spatial resolution, while both PTFE and PE interfaces are over-smoothed, the latter yielding the worst spatial resolution. To allow for a visual comparison the test object's images reconstructed with FBP, SART, cSART within and out from the threshold condition are reported in Fig. S3 and Fig. S4 of the supplementary material.

3.2. Breast specimen

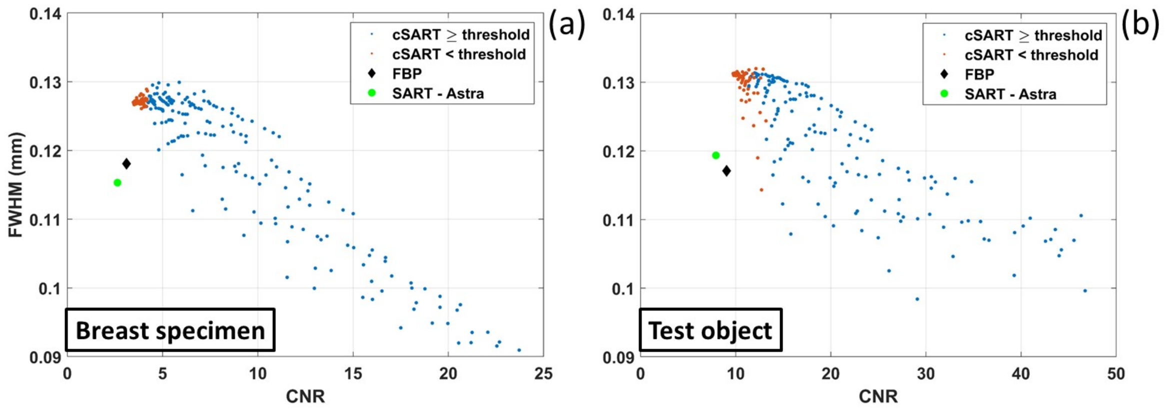

Figure 6. Scatter plots of FWHM (measured with Mitzutani's method) versus CNR for the breast specimen (a) and for PTFE insert in the test object (b). Orange and blue points indicate cSART reconstructions within and out from the NPS peak threshold condition, while black diamond and green circle indicate FBP and SART.

3.2.1. Texture, contrast-to-noise and spatial resolution A qualitative comparison on a detail of the breast sample centered on the tumor mass is shown in Fig. 5; in panel (a) the reference image acquired at high radiation dose (50 mGy) is reported, while from (b) to (e) there are the images acquired with the standard 5 mGy dose and reconstructed through FBP (b), standard SART (c), cSART within the threshold condition (d) ($\sigma_{xy,z} = 2$, $\sigma_v = 0.008$ and $\cancel{\eta}$ $w = 0.06$) and out from the threshold condition (e) ($\sigma_{xy,z} = 7$, $\sigma_v = 0.014$ and $\cancel{\eta}$ $w = 0.08$). As expected from the photon statistics, going from the high to the low dose images reconstructed via FBP a 3-fold decrease in CNR is observed (from 9.2 to 3.1). On the other hand, no advantage over FBP in terms of image quality is associated with the use of conventional SART, while the cSART image satisfying the threshold criterion features a higher CNR (4.2), similar texture and no apparent spatial resolution degradation. Interestingly, as shown in (e), by increasing the cSART parameters an image with the same CNR observed in the reference high dose image (CNR = 9.2) can be obtained at cost of an increased patchiness. The corresponding images of the whole sample are reported in Fig. S5 of the supplementary material.

The quantitative analysis on the specimen images is reported in Fig. 6. In particular, panel (a) shows the FWHM, evaluated with Mizutani's approach, as a function of CNR measured on the breast specimen for cSART, FBP and SART reconstructions. Similar to the test object's case, the cSART reconstructions satisfying the NPS frequency peak threshold criterion, yield a higher CNR (up to 35%) if compared to FBP, with only a marginal degradation (below 10%) in the spatial resolution. On the other hand, the standard SART reconstruction yields a spatial resolution comparable with FBP but with a 15% lower CNR. In absolute terms, the mean FWHM of cSART reconstructions satisfying the threshold condition is 0.13 mm, whereas for the FBP case it as around 0.12 mm. The latter value is in good agreement with previous

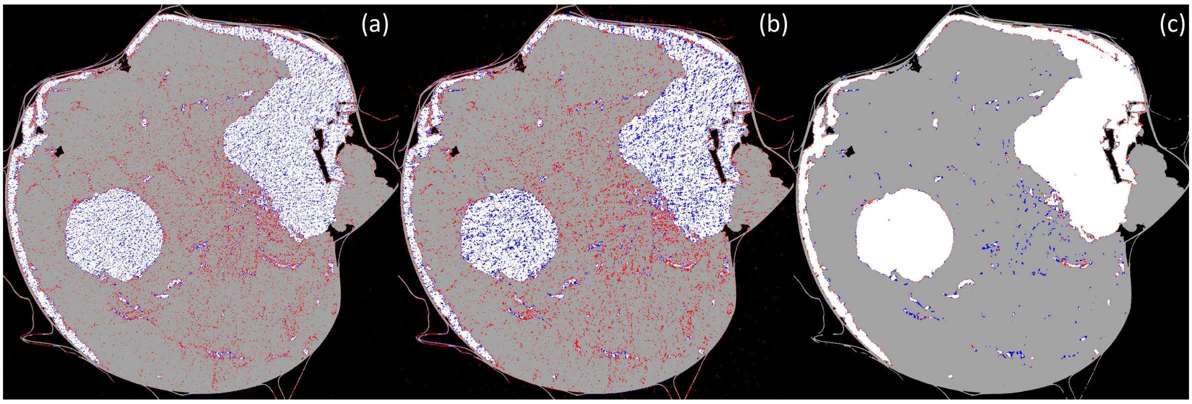

Figure 7. Segmented components of the FBP at 50 mGy shown overlapped with those of the FBP at 5 mGy (a), standard SART (b) and cSART at highest F1 score (c). Air background is shown in black, adipose component in gray, glandular component in white and misclassified pixels in ~~green~~ blue and ~~magenta~~ red.

measurements performed with the same imaging setup on different samples (Brombal et al. 2019, Brombal et al. 2018a, Donato et al. 2019b), and it corresponds roughly to twice the detector's pixel size. Interestingly, when applying the Mizutani's approach to the test object, similar spatial resolution values are observed, as shown in panel (b). As mentioned, this approach aims at evaluating the overall spatial resolution of the imaging system, therefore it is expected that the FWHM does not change by changing the sample.

3.2.2. Image segmentation Qualitative results of the image segmentation are showed in Fig.7. Panels (a)-(c) show the overlay of the segmented ground-truth image with the segmented FBP (a), standard SART (b) and cSART at highest F1 (c) images. The three components of the segmentation, namely the air background, adipose and glandular tissue are showed, respectively, in black, gray and white. ~~Green~~ Blue and ~~magenta~~ red pixels are the misclassified pixels of adipose and glandular classes, respectively (~~green~~ blue is glandular classified as adipose and ~~magenta~~ red is vice versa). From the images it is clear that, when compared to the reference high-dose image, the cSART algorithm with adequately tuned parameters largely outperforms the FBP-based segmented image.

The quantitative analysis on the segmented images is reported in the plots of Fig. 8. In panel (a)-(c) the optimization of the segmentation threshold between glandular and adipose components for different cSART parameters combinations is reported. The optimal threshold was found to be loosely independent from the reconstruction parameters and, in all cases, was around 0.21. Considering the effect of each cSART parameter on segmentation quality, panel (a) demonstrates that F1 increases at higher σ_v values reaching a plateau for $\sigma_v > 0.014$. Conversely, panel (b) shows that higher F1 scores are related to lower $\sigma_{xy,z}$, hence to small spatial blurring which contributes to the preservation of fine details. Finally, panel (c) shows that F1 peaks for intermediate

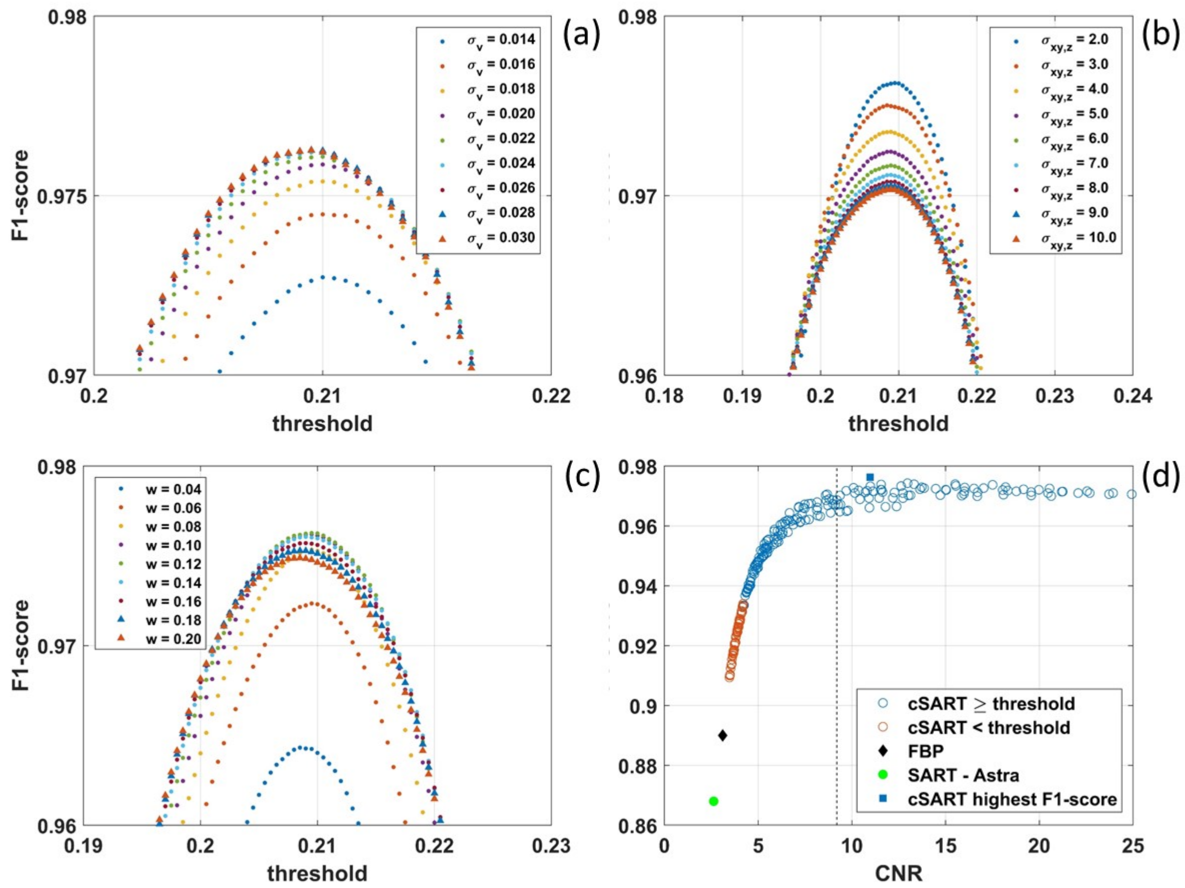

Figure 8. F1 score as a function of the adipose-glandular threshold th for: $\cancel{\eta = 0.14}$ $w = 0.12$, $\sigma_{xy,z} = 2.0$ and different values for σ_v (a); $\cancel{\eta = 0.14}$ $w = 0.12$, $\cancel{\sigma_v = 0.020}$ $\sigma_v = 0.028$ and different values for $\sigma_{xy,z}$ (b); $\sigma_{xy,z} = 2.0$, $\cancel{\sigma_v = 0.020}$ $\sigma_v = 0.028$ and different values for $\cancel{\eta}$ w (c). Panel (d) shows F1 as a function of the CNR where orange and blue open circles indicate cSART reconstructions within and out from the NPS peak threshold condition, black diamond is FBP, green circle is SART. The blue square indicates cSART yielding the highest F1 score. The dashed vertical line represents the CNR value of the FBP reconstructed reference image at 50 mGy.

values of $\cancel{\eta}$ w. In panel (d) the F1 scores are plotted against the respective CNR values, also including the FBP and SART reconstructions. The plot indicates that cSART reconstructions always result in a better segmentation with respect to FBP and SART. Moreover, it is interesting to observe that a higher fidelity in the segmentation is achieved for cSART reconstructions not comprised within the NPS frequency peak threshold condition, ~~confirming that the optimization of reconstruction parameters for segmentation is different from the one for diagnostic visualization~~ indicating that optimal parameters for segmentation are different with respect to the ones for diagnostic visualization. The plot also indicates that when the cSART images reach the same CNR as the reference image (dashed line in the plot) the segmentation quality saturates and there is no advantage in pursuing higher CNR values. In addition, segmentation results obtained with the cSART algorithm for different numbers of iterations, from 4 to 8, are reported in Fig. S6 of the supplementary material and in the supplementary table 1. The results show that the highest F1-score corresponds to 5 iterations, while neither the optimal $\sigma_{xy,z}$ nor the optimal σ_v are dependent on the number of iterations. On the other hand, when increasing the number of iterations, the optimal weighting factor w tends to decrease.

4. Conclusions

This study shows that the adoption of iterative reconstruction techniques can provide significant advantages in the context of breast CT imaging with monochromatic synchrotron radiation and using free-space propagation and phase-retrieval. In particular, based on images of a surgical breast sample, the use of the customized GPU-based SART algorithm herein presented resulted in a contrast to noise ratio gain up to 35% with an only marginal decrease in spatial resolution (less than 10%) and image texture properties similar to the reference FBP case. Analogous indications were obtained from the analysis on the dedicated test object, revealing a CNR gain from 45% to 100% across different plastic inserts at a comparable or slightly worse spatial resolution and similar NPS peak frequency (difference less than 15%) when compared with FBP. On the other hand, the use of standard SART algorithm did not provide any advantage over FBP, generally resulting in noisier images and a coarser noise structure. A threshold for NPS frequency peak was used as first line discrimination criterion to identify those cSART parameters that preserve the image texture when compared to FBP. In this study the threshold was arbitrarily set to 15% but, in the future, its definition will be subject to a dedicated reader study. It is worth noting that the triplets of parameters satisfying the threshold condition for the test object overlap with those for the breast specimen. ~~This suggests that the phantom based optimization of the cSART algorithm is representative for the breast specimen.~~

Moreover, the presence of sharp plastic inserts in the phantom allowed for a task transfer function (TTF) analysis, resulting in different trends in the spatial resolution for different materials. This finding further confirms the need for careful optimization of IR algorithms as their performances are dependent on the imaged object, plus it suggests the usefulness of test objects closely reproducing the contrast characteristics of the investigated organ. When the latter condition is satisfied, the similar trends observed in terms of CNR and spatial resolution for breast tissue and the test object, suggest that the optimization of the cSART algorithm can be carried out based on test object images, therefore being feasible virtually in any clinical system. It should be stressed that this indication would need to be confirmed by scanning a larger number of samples in different experimental conditions and focusing on specific features of clinical interest (e.g., microcalcifications or margins sharpness), which will be the subject of future studies. In this context, a dedicated investigation on cSART reconstructed images at coarser angular stepping will be performed with the aim of reducing the scan time and

(optionally) the radiation dose.
~~Additionally,~~ The study also demonstrated that the proposed algorithm offers great flexibility, ~~allowing to optimize image reconstruction either towards diagnostic evaluation, with a limited gain in CNR and textural properties similar to FBP, or towards image segmentation, with a major gain in CNR (by a factor of 3 or more) at cost of increased image patchiness~~ allowing to optimize image reconstruction either for diagnostic evaluation images (limited CNR gain and textural properties similar to FBP) or for image segmentation (major CNR gain and increase patchiness). The latter feature is of great importance as it would enable, starting from low dose clinical images, for accurate glandular fraction estimation and straightforward realization of 3D breast models.

Aknowledgment

This research has been supported by the "AIM: Attraction and International Mobility"-PON R&I 2014-2020 Calabria.

References

Bartels, M. (2013). *Cone-beam X-ray phase contrast tomography of biological samples: optimization of contrast, resolution and field of view*, Vol. 13, Universitätsverlag Göttingen.

Bellazzini, R., Spandre, G., Brez, A., Minuti, M., Pinchera, M. & Mozzo, P. (2013). Chromatic X-ray imaging with a fine pitch CdTe sensor coupled to a large area photon counting pixel ASIC, *Journal of Instrumentation* **8**(02): C02028.

Beltran, M. A., Paganin, D., Uesugi, K. & Kitchen, M. J. (2010). 2D and 3D X-ray phase retrieval of multi-material objects using a single defocus distance, *Optics Express* **18**(7): 6423–6436.

Bian, J., Yang, K., Boone, J. M., Han, X., Sidky, E. Y. & Pan, X. (2014). Investigation of iterative image reconstruction in low-dose breast ct, *Physics in Medicine & Biology* **59**(11): 2659.

Brombal, L. (2020a). Effectiveness of X-ray phase-contrast tomography: effects of pixel size and magnification on image noise, *Journal of Instrumentation* **15**(01): C01005.

Brombal, L. (2020b). *X-ray Phase-Contrast Tomography*, Springer Theses, Springer International Publishing.

Brombal, L., Arana Peña, L. M., Arfelli, F., Longo, R., Brun, F., Contillo, A., Di Lillo, F., Tromba, G., Di Trapani, V., Donato, S. et al. (2021). Motion artifacts assessment and correction using optical tracking in synchrotron radiation breast ct, *Medical Physics* .

Brombal, L., Arfelli, F., Delogu, P., Donato, S., Mettivier, G., Michielsen, K., Oliva, P., Taibi, A., Sechopoulos, I., Longo, R. & Fedon, C. (2019). Image quality comparison between a phase-contrast synchrotron radiation breast CT and a clinical breast CT: a phantom based study, *Scientific reports* **9**(1): 1–12.

Brombal, L., Donato, S., Brun, F., Delogu, P., Fanti, V., Oliva, P., Rigon, L., Di Trapani, V., Longo, R. & Golosio, B. (2018c). Large-area single-photon-counting CdTe detector for synchrotron radiation computed tomography: a dedicated pre-processing procedure, *Journal of synchrotron radiation* **25**(4).

Brombal, L., Donato, S., Dreossi, D., Arfelli, F., Bonazza, D., Contillo, A., Delogu, P., Di Trapani, V., Golosio, B., Mettivier, G., Oliva, P., Rigon, L., Taibi, A. & Longo, R. (2018a). Phase-contrast breast ct: the effect of propagation distance, *Physics in Medicine & Biology* **63**(24): 24NT03.

Brombal, L., Golosio, B., Arfelli, F., Bonazza, D., Contillo, A., Delogu, P., Donato, S., Mettivier, G., Oliva, P., Rigon, L., Taibi, A., Tromba, G., Zanconati, F. & Longo, R. (2018b). Monochromatic breast computed tomography with synchrotron radiation: phase-contrast and phase-retrieved image comparison and full-volume reconstruction, *Journal of Medical Imaging* **6**(3): 031402.

Caballo, M., Fedon, C., Brombal, L., Mann, R., Longo, R. & Sechopoulos, I. (2018). Development of 3D patient-based super-resolution digital breast phantoms using machine learning, *Physics in Medicine & Biology* **63**(22): 225017.

Chen, B., Christianson, O., Wilson, J. M. & Samei, E. (2014b). Assessment of volumetric noise and resolution performance for linear and nonlinear CT reconstruction methods, *Medical physics* **41**(7): 071909.

Chen, B. & Ning, R. (2002). Cone-beam volume CT breast imaging: Feasibility study, *Medical physics* **29**(5): 755–770.

Chen, B., Ramirez Giraldo, J. C., Solomon, J. & Samei, E. (2014a). Evaluating iterative reconstruction performance in computed tomography, *Medical physics* **41**(12): 121913.

Sidky, E. Y. & Pan, X. (2008). Image reconstruction in circular cone-beam computed tomography by constrained, total-variation minimization, *Physics in Medicine & Biology* **53**(17): 4777.

Baran, P., Pacile, S., Nesterets, Y. I., Mayo, S., Dullin, C., Dreossi, D., Arfelli, F., Thompson, D., Lockie, D., McCormack, M. et al. (2017). Optimization of propagation-based x-ray phase-contrast tomography for breast cancer imaging, *Physics in Medicine & Biology* **62**(6): 2315.

Contillo, A., Veronese, A., Brombal, L., Donato, S., Rigon, L., Taibi, A., Tromba, G., Longo, R. & Arfelli, F. (2018). A proposal for a quality control protocol in breast CT with synchrotron radiation, *Radiology and oncology* **52**(3): 329–336.

Delogu, P., Brombal, L., Di Trapani, V., Donato, S., Bottigli, U., Dreossi, D., Golosio, B., Oliva, P., Rigon, L. & Longo, R. (2017b). Optimization of the equalization procedure for a single-photon counting CdTe detector used for CT, *Journal of Instrumentation* **12**(11): C11014.

Delogu, P., Di Trapani, V., Brombal, L., Mettivier, G., Taibi, A. & Oliva, P. (2019). Optimization of the energy for breast monochromatic absorption X-ray Computed Tomography, *Scientific reports* **9**(1): 1–10.

Delogu, P., Golosio, B., Fedon, C., Arfelli, F., Bellazzini, R., Brez, A., Brun, F., Di Lillo, F., Dreossi, D., Mettivier, G. et al. (2017a). Imaging study of a phase-sensitive breast-ct system in continuous acquisition mode, *Journal of Instrumentation* **12**(01): C01016.

Donato, S., Brombal, L., Arfelli, F., Fanti, V., Longo, R., Oliva, P., Rigon, L. & Golosio, B. (2019a). Optimization of a customized simultaneous algebraic reconstruction technique algorithm for breast ct, *2019 IEEE Nuclear Science Symposium and Medical Imaging Conference (NSS/MIC)*, IEEE, pp. 1–2.

Donato, S., Pacilè, S., Brombal, L., Tromba, G. & Longo, R. (2019b). Phase-contrast breast-CT: optimization of experimental parameters and reconstruction algorithms, *World Congress on Medical Physics and Biomedical Engineering 2018*, Springer, pp. 109–115.

Euler, A., Solomon, J., Marin, D., Nelson, R. C. & Samei, E. (2018). A third-generation adaptive statistical iterative reconstruction technique: phantom study of image noise, spatial resolution, lesion detectability, and dose reduction potential, *American Journal of Roentgenology* pp. 1301–1308.

Fedon, C., Longo, F., Mettivier, G. & Longo, R. (2015). GEANT4 for breast dosimetry: parameters optimization study, *Physics in Medicine & Biology* **60**(16): N311.

Germann, M., Shim, S., Angst, F., Saltybaeva, N. & Boss, A. (2020). Spiral breast computed tomography (CT): signal-to-noise and dose optimization using 3D-printed phantoms, *European Radiology* pp. 1–10.

Gervaise, A., Osemont, B., Lecocq, S., Noel, A., Micard, E., Felblinger, J. & Blum, A. (2012). CT image quality improvement using adaptive iterative dose reduction with wide-volume acquisition on 320-detector CT, *European radiology* **22**(2): 295–301.

Ghetti, C., Palleri, F., Serreli, G., Ortenzia, O. & Ruffini, L. (2013). Physical characterization of a new CT iterative reconstruction method operating in sinogram space, *Journal of applied clinical medical physics* **14**(4): 263–271.

Golosio, B., Brunetti, A. & Cesareo, R. (2004). Algorithmic techniques for quantitative compton tomography, *Nuclear Instruments and Methods in Physics Research Section B: Beam Interactions with Materials and Atoms* **213**: 108–111.

Gordon, R., Bender, R. & Herman, G. T. (1970). Algebraic reconstruction techniques (art) for three-dimensional electron microscopy and X-ray photography, *Journal of theoretical Biology* **29**(3): 471–481.

Greffier, J., Macri, F., Larbi, A., Fernandez, A., Khasanova, E., Pereira, F., Mekkaoui, C. & Beregi, J. (2015). Dose reduction with iterative reconstruction: optimization of CT protocols in clinical practice, *Diagnostic and interventional imaging* **96**(5): 477–486.

Gureyev, T. E., Nesterets, Y. I., Kozlov, A., Paganin, D. M. & Quiney, H. M. (2017). On the "unreasonable" effectiveness of transport of intensity imaging and optical deconvolution, *JOSA A* **34**(12): 2251–2260.

Gureyev, T., Nesterets, Y. I., Baran, P., Taba, S., Mayo, S., Thompson, D., Arhatari, B., Mihocic, A., Abbey, B., Lockie, D., Fox, J., Kumar, B., Prodanovic, Z., Hausermann, D., Maksimenko, A., Hall, C., Peele, A., Dimmock, M., Pavlov, K., Cholewa, M., Lewis, S., Tromba, G., Quiney, H. & Brennan, P. (2019). Propagation-based X-ray phase-contrast tomography of mastectomy samples using synchrotron radiation, *Medical physics* **46**(12): 5478–5487.

Kak, A. C., Slaney, M. & Wang, G. (2002). Principles of computerized tomographic imaging.

Kalender, W. A., Kolditz, D., Steiding, C., Ruth, V., Lück, F., Rößler, A.-C. & Wenkel, E. (2017). Technical feasibility proof for high-resolution low-dose photon-counting CT of the breast, *European radiology* **27**(3): 1081–1086.

Li, K., Garrett, J., Ge, Y. & Chen, G.-H. (2014). Statistical model based iterative reconstruction (mbir) in clinical CT systems. part ii. experimental assessment of spatial resolution performance, *Medical physics* **41**(7): 071911.

Lindfors, K. K., Boone, J. M., Nelson, T. R., Yang, K., Kwan, A. L. & Miller, D. F. (2008). Dedicated breast ct: initial clinical experience, *Radiology* **246**(3): 725–733.

Lindfors, K. K., Boone, J. M., Newell, M. S. & D'Orsi, C. J. (2010). Dedicated breast computed tomography: the optimal cross-sectional imaging solution?, *Radiologic Clinics* **48**(5): 1043–1054.

Lipton, Z. C., Elkan, C. & Naryanaswamy, B. (2014). Optimal thresholding of classifiers to maximize F1 measure, *Joint European Conference on Machine Learning and Knowledge Discovery in Databases*, Springer, pp. 225–239.

Longo, R., Arfelli, F., Bonazza, D., Bottigli, U., Brombal, L., Contillo, A., Cova, M. A., Delogu, P., Di Lillo, F., Di Trapani, V., Donato, S., Dreossi, D., Fanti, V., Fedon, C., Golosio, B., Mettivier, G., Oliva, P., Pacilè, S., Sarno, A., Rigon, L., Russo, P., Taibi, A., Tonutti, M., Zanconati, F. & Tromba, G. (2019). Advancements towards the implementation of clinical phase-contrast breast computed tomography at Elettra, *Journal of Synchrotron Radiation* **26**(4).

Löve, A., Olsson, M., Siemund, R., Stålhammar, F., Björkman-Burtscher, I. & Söderberg, M. (2013). Six iterative reconstruction algorithms in brain CT: a phantom study on image quality at different radiation dose levels, *The British journal of radiology* **86**(1031): 20130388.

Makeev, A. & Glick, S. J. (2013). Investigation of statistical iterative reconstruction for dedicated breast CT, *Medical Physics* **40**(8): 081904.

Mettivier, G., Fedon, C., Di Lillo, F., Longo, R., Sarno, A., Tromba, G. & Russo, P. (2015). Glandular dose in breast computed tomography with synchrotron radiation, *Physics in Medicine & Biology* **61**(2): 569.

Miéville, F. A., Gudinchet, F., Brunelle, F., Bochud, F. O. & Verdun, F. R. (2013). Iterative reconstruction methods in two different MDCT scanners: physical metrics and 4-alternative forced-choice detectability experiments–a phantom approach, *Physica medica* **29**(1): 99–110.

Mirone, A., Brun, E. & Coan, P. (2014). A dictionary learning approach with overlap for the low dose computed tomography reconstruction and its vectorial application to differential phase tomography, *PloS one* **9**(12): e114325.

Mittone, A., Bravin, A. & Coan, P. (2018). Low-dose quantitative phase contrast medical CT, *Measurement Science and Technology* **29**(2): 024006.

Mizutani, R., Saiga, R., Takekoshi, S., Inomoto, C., Nakamura, N., Itokawa, M., Arai, M., Oshima, K., Takeuchi, A., Uesugi, K., Terada, Y. & Suzuki, Y. (2016). A method for estimating spatial resolution of real image in the Fourier domain, *Journal of microscopy* **261**(1): 57–66.

Nishiyama, Y., Tada, K., Nishiyama, Y., Mori, H., Maruyama, M., Katsube, T., Yamamoto, N., Kanayama, H., Yamamoto, Y. & Kitagaki, H. (2016). Effect of the forward-projected model-based iterative reconstruction solution algorithm on image quality and radiation dose in pediatric cardiac computed tomography, *Pediatric radiology* **46**(12): 1663–1670.

O'Connell, A., Conover, D. L., Zhang, Y., Seifert, P., Logan-Young, W., Lin, C.-F. L., Sahler, L. & Ning, R. (2010). Cone-beam CT for breast imaging: Radiation dose, breast coverage, and image quality, *American Journal of Roentgenology* **195**(2): 496–509.

Oliva, P., Di Trapani, V., Arfelli, F., Brombal, L., Donato, S., Golosio, B., Longo, R., Mettivier, G., Rigon, L., Taibi, A., Tromba, G., Zanconati, F. & Delogu, P. (2020). Experimental optimization of the energy for breast-CT with synchrotron radiation, *Scientific reports* **10**(1): 1–13.

Oliva, P., Golosio, B., Arfelli, F., Delogu, P., Di Lillo, F., Dreossi, D., Fanti, V., Fardin, L., Fedon, C., Mettivier, G., Rigon, L., Russo, P., Sarno, A., Tromba, G. & Longo, R. (2017). Quantitative evaluation of breast CT reconstruction by means of figures of merit based on similarity metrics, *2017 IEEE Nuclear Science Symposium and Medical Imaging Conference (NSS/MIC)*, IEEE, pp. 1–5.

Opitz, J. & Burst, S. (2019). Macro F1 and macro F1, *arXiv preprint arXiv:1911.03347v2* .

O'Connell, A. M., Karellas, A., Vedantham, S. & Kawakyu-O'Connor, D. T. (2018). Newer technologies in breast cancer imaging: dedicated cone-beam breast computed tomography, *Seminars in Ultrasound, CT and MRI*, Vol. 39, Elsevier, pp. 106–113.

Pacilè, S., Brun, F., Dullin, C., Nesterets, Y., Dreossi, D., Mohammadi, S., Tonutti, M., Stacul, F., Lockie, D., Zanconati, F., Accardo, A., Tromba, G. & Gureyev, T. E. (2015). Clinical application of low-dose phase contrast breast CT: methods for the optimization of the reconstruction workflow, *Biomedical optics express* **6**(8): 3099–3112.

Pacilè, S., Dullin, C., Baran, P., Tonutti, M., Perske, C., Fischer, U., Albers, J., Arfelli, F., Dreossi, D., Pavlov, K., Maksimenko, A., Mayo, S., Nesterets, Y., Tavakoli Taba, S., Lewis, S., Brennan, P., Gureyev, T., Tromba, G. & Wienbec, S. (2019). Free propagation phase-contrast breast ct provides higher image quality than cone-beam breast-ct at low radiation doses: a feasibility study on human mastectomies, *Scientific reports* **9**(1): 1–7.

Paganin, D., Mayo, S. C., Gureyev, T. E., Miller, P. R. & Wilkins, S. W. (2002). Simultaneous phase and amplitude extraction from a single defocused image of a homogeneous object, *Journal of microscopy* **206**(1): 33–40.

Piai, A., Contillo, A., Arfelli, F., Bonazza, D., Brombal, L., Cova, M. A., Delogu, P., Di Trapani, V., Donato, S., Golosio, B., Mettivier, G., Oliva, P., Rigon, L., Taibi, A., Tonutti, M., Tromba, G. & Zanconati, F. (2019). Quantitative characterization of breast tissues with dedicated CT imaging, *Physics in Medicine & Biology* .

Richard, S., Husarik, D. B., Yadava, G., Murphy, S. N. & Samei, E. (2012). Towards task-based assessment of CT performance: system and object MTF across different reconstruction algorithms, *Medical physics* **39**(7Part1): 4115–4122.

Saiga, R., Takeuchi, A., Uesugi, K., Terada, Y., Suzuki, Y. & Mizutani, R. (2018). Method for estimating modulation transfer function from sample images, *Micron* **105**: 64–69.

Sarno, A., Mettivier, G. & Russo, P. (2015). Dedicated breast computed tomography: basic aspects, *Medical physics* **42**(6Part1): 2786–2804.

Schulz, B., Beeres, M., Bodelle, B., Bauer, R., Al-Butmeh, F., Thalhammer, A., Vogl, T. & Kerl, J. (2013). Performance of iterative image reconstruction in CT of the paranasal sinuses: a phantom study, *American Journal of Neuroradiology* **34**(5): 1072–1076.

Shim, S., Saltybaeva, N., Berger, N., Marcon, M., Alkadhi, H. & Boss, A. (2020). Lesion detectability and radiation dose in spiral breast CT with photon-counting detector technology: A phantom study, *Investigative radiology* **55**(8): 515–523.

Sidky, E. Y., Chartrand, R., Boone, J. M. & Pan, X. (2014). Constrained *TpV* minimization for enhanced exploitation of gradient sparsity: Application to CT image reconstruction, *IEEE journal of translational engineering in health and medicine* **2**: 1–18.

Solomon, J., Marin, D., Roy Choudhury, K., Patel, B. & Samei, E. (2017). Effect of radiation dose reduction and reconstruction algorithm on image noise, contrast, resolution, and detectability of subtle hypoattenuating liver lesions at multidetector CT: filtered back projection versus a commercial model–based iterative reconstruction algorithm, *Radiology* **284**(3): 777–787.

Solomon, J., Wilson, J. & Samei, E. (2015). Characteristic image quality of a third generation dual-source MDCT scanner: noise, resolution, and detectability, *Medical physics* **42**(8): 4941–4953.

Taylor, J. A. (2018). TS imaging.
URL: *http://ts-imaging.science.unimelb.edu.au/Services/Simple/*

Thompson, D. A., Nesterets, Y. I., Pavlov, K. M. & Gureyev, T. E. (2019). Fast three-dimensional phase retrieval in propagation-based X-ray tomography, *Journal of synchrotron radiation* **26**(3): 825–838.

Tromba, G., Longo, R., Abrami, A., Arfelli, F., Astolfo, A., Bregant, P., Brun, F., Casarin, K., Chenda, V., Dreossi, D., Hola, M., Kaiser, J., Mancini, L., Menk, R., Quai, E., Quaia, E., Rigon, L., Rokvic, T., Sodini, N., Sanabor, D., Schultke, E., Tonutti, M., Vascotto, A., Zanconati, F., Cova, M. & Castelli, E. (2010). The syrmep beamline of elettra: Clinical mammography and bio-medical applications, *AIP Conference Proceedings*, Vol. 1266, AIP, pp. 18–23.

Tseng, H. W., Vedantham, S. & Karellas, A. (2020). Cone-beam breast computed tomography using ultra-fast image reconstruction with constrained, total-variation minimization for suppression of artifacts, *Physica Medica* **73**: 117–124.

Van Aarle, W., Palenstijn, W. J., Cant, J., Janssens, E., Bleichrodt, F., Dabravolski, A., De Beenhouwer, J., Batenburg, K. J. & Sijbers, J. (2016). Fast and flexible X-ray tomography using the Astra toolbox, *Optics express* **24**(22): 25129–25147.

Verdun, F., Racine, D., Ott, J., Tapiovaara, M., Toroi, P., Bochud, F., Veldkamp, W., Schegerer, A., Bouwman, R., Giron, I. H., Marshall, N. & Edyvean, S. (2015). Image quality in CT : From physical measurements to model observers, *Physica Medica* **31**(8): 823–843.

White, D., Booz, J., Griffith, R., Spokas, J. & Wilson, I. (1989). Tissue substitutes in radiation dosimetry and measurement, report 44, *International Commission on Radiation Units & Measurements, Bethesda, MD, USA https://doi. org/10.1093/jicru/os23* **1**.

Wienbeck, S., Lotz, J. & Fischer, U. (2017). Review of clinical studies and first clinical experiences with a commercially available cone-beam breast CT in europe, *Clinical imaging* **42**: 50–59.

Wilkins, S., Gureyev, T. E., Gao, D., Pogany, A. & Stevenson, A. (1996). Phase-contrast imaging using polychromatic hard X-rays, *Nature* **384**(6607): 335–338.

Willemink, M. J., Leiner, T., de Jong, P. A., de Heer, L. M., Nievelstein, R. A., Schilham, A. M. & Budde, R. P. (2013). Iterative reconstruction techniques for computed tomography part 2: initial results in dose reduction and image quality, *European radiology* **23**(6): 1632–1642.

Wu, X.-Z. & Zhou, Z.-H. (2017). A unified view of multi-label performance measures, *International Conference on Machine Learning*, PMLR, pp. 3780–3788.

Zhao, Y., Brun, E., Coan, P., Huang, Z., Sztrókay, A., Diemoz, P. C., Liebhardt, S., Mittone, A., Gasilov, S., Miao, J. & Bravin, A. (2012). High-resolution, low-dose phase contrast X-ray tomography for 3D diagnosis of human breast cancers, *Proceedings of the National Academy of Sciences* **109**(45): 18290–18294.